

Learning Differentiable Weak-Form Corrections to Accelerate Finite Element Simulations

Junoh Jung^{*1} and Emil Constantinescu¹

¹Mathematics and Computer Science Division, Argonne National Laboratory, Lemont 60439 IL, USA

Abstract. We present a differentiable weak-form learning approach for accelerating finite element simulations. Rather than introducing black-box source terms in the strong form of the governing equations, we augment the momentum equation directly in the variational (weak) form with parameterized bilinear operators. The coefficients of these operators are learned from high-resolution simulations so that unresolved small-scale dynamics can be represented on coarse grids. Applying the correction at the weak-form level aligns the learned model with the finite element discretization, preserving key numerical structure and better respecting the fundamental properties of incompressible flow. In the same setting, the approach yields solutions that are more accurate and more stable over long time horizons than comparable strong-form corrections. We implement the proposed method in the Firedrake finite element solver and evaluate it on benchmark problems, including the one-dimensional convection–diffusion equation and the two-dimensional incompressible Navier–Stokes equations. End-to-end differentiable training is enabled by coupling PyTorch with the Firedrake adjoint framework. Across these tests, the learned variational operators improve long-term accuracy while reducing computational cost. Overall, our results suggest that weak-form learning provides a principled, structure-preserving route to accurate and stable coarse-grid simulations of incompressible flows.

1 Introduction

In the era of artificial intelligence, recent advances in machine learning (ML) have opened complementary avenues for fluid simulation. Purely data-driven surrogates—ranging from physics-informed neural networks (PINNs) to operator-learning architectures and mesh-graph networks—can emulate partial differential equation (PDE) solvers and deliver impressive speedups. However, ensuring long-horizon stability, conservation, and generalization to out-of-distribution regimes remains challenging for end-to-end modeling. Representative contributions include the review by [Brunton et al. \[2020\]](#) on machine learning for fluid mechanics, the physics-informed neural network (PINN) framework introduced by [Raissi et al. \[2019\]](#), operator-learning approaches such as the Fourier neural operator (FNO) [[Li et al., 2021](#)], graph-based surrogate modeling exemplified by MeshGraphNets [[Pfaff et al., 2021](#)], and data-driven global weather forecasting with Four-CastNet [[Pathak et al., 2022](#)].

A promising alternative is hybrid physics–ML modeling, in which learned components are embedded within established PDE solvers to enhance accuracy and efficiency while preserving numerical structure. Prior efforts span learning discretizations [[Bar-Sinai et al., 2019](#)], subgrid closures for large eddy simulation

^{*}Email address for correspondence: jjung@anl.gov

[Beck et al., 2019, Maulik et al., 2019, Xie et al., 2020], Reynolds-averaged Navier–Stokes corrections with invariance [Ling et al., 2016], and field-inversion-and-ML approaches for model-consistent augmentation [Parish and Duraisamy, 2016, Singh and Duraisamy, 2017]. Embedding ML inside the solver has been shown to improve accuracy at lower cost by leveraging the structure of the underlying numerical scheme. In compressible flows, recent work has accelerated discontinuous Galerkin (DG) solvers using learned correction terms with discrete updates [De Lara and Ferrer, 2022, Otmani et al., 2025], and Kang and Constantinescu [2025] further generalized the approach in DG and introduced continuous corrections via neural operators. Similar work was extended to a large-scale problem in a supercomputer setting [Jung and Constantinescu, 2025]. Despite this progress, few studies have examined learned corrections tailored to incompressible solvers on coarse grids, where maintaining stable long-time behavior is critical.

End-to-end learning in hybrid physics–ML computational fluid dynamics (CFD) refers to optimizing a learnable component (e.g., a closure or correction term) through the numerical solver against a global objective, such as mismatch in state variables, integral loads, or statistical quantities, so that training remains consistent with both the governing equations and their discrete time-marching implementation [Vinuesa and Brunton, 2022, Sanderse et al., 2025]. When high-fidelity labels for the unclosed term are available (e.g., filtered subgrid stresses or eddy viscosity), a common alternative is a priori supervised training performed outside the CFD loop, which avoids the need to differentiate through the full solver trajectory [Sanderse et al., 2025]. However, many practical settings provide only indirect supervision (sparse measurements, pressure/velocity probes, forces, or long-time statistics). In this regime, end-to-end (embedded) training places the CFD solver in the loop and requires gradients of the objective with respect to ML parameters through the full discretized algorithm [Michelén and Xiao, 2021, Sirignano et al., 2020, MacArt et al., 2021, Shankar et al., 2025]. These sensitivities can be obtained via discrete adjoint formulations and via automatic differentiation of a differentiable solver, both of which remain nontrivial for large-scale unsteady CFD [Michelén and Xiao, 2021, Bezgin et al., 2023, 2025]. Recent studies nevertheless demonstrate that solver-consistent training can materially improve stability and long-horizon accuracy of learned closures and hybrid architectures, including implementations on complex geometries and unstructured grids [De Avila Belbute-Peres et al., 2020, List et al., 2022, Kim et al., 2024].

Firedrake [Ham et al., 2023] is an automated finite element framework for the solution of PDEs using solvers based on the Portable, Extensible Toolkit for Scientific Computation (PETSc) [Balay et al., 2019], which can provide a natural entry point for differentiable PDE programs at the level of weak forms [Rathgeber et al., 2016]. Its adjoint capability (firedrake.adjoint) builds on the pyadjoint approach [Mitusch et al., 2019]. Specifically, the forward model is annotated (“taped”), and then discrete tangent-linear/adjoint models are derived and solved automatically, enabling scalable gradient evaluation for PDE-constrained optimization and inverse problems [Farrell et al., 2013, Mitusch et al., 2019, Funke and Farrell, 2013]. This differentiable foundation has been exercised extensively in gradient-based inference workflows built on Firedrake, including recent work that introduces a composable and differentiable point-evaluation abstraction for consistent data assimilation in Firedrake/Icepack [Nixon-Hill et al., 2024]. Firedrake’s differentiable programming story also has been extended explicitly toward hybrid physics–ML training. A foreign-function/external-operator interface was introduced so that operators not representable in pure United Form Language vector calculus, such as neural network closures implemented in PyTorch, can appear directly inside variational forms while remaining compatible with assembly and adjoint differentiation [Bouziani and Ham, 2021]. Building on these ideas, subsequent interfaces couple Firedrake with mainstream ML components by wrapping Firedrake computations as custom operators for PyTorch, thereby enabling end-to-end training of coupled PDE-neural models using standard deep-learning optimizers while still leveraging Firedrake’s code-generated performance and adjoint machinery [Bouziani and Ham, 2023, Bouziani et al., 2024].

Beyond strong-form correction, a growing body of work in scientific ML emphasizes variational/weak-form learning, coupling data-driven components to the same integrated, test-function–weighted equations that underlie Galerkin finite elements and many projection-based reduced-order models. Recent efforts have used

weak forms as the interface for learned correction/closure operators: in variational multiscale reduced-order models, neural networks learn the influence of unresolved scales while preserving Galerkin structure and energy/consistency properties [Mou et al., 2021, Ahmed et al., 2023, Dar et al., 2023, Ivagnes et al., 2023, Koc et al., 2025]. Related work embeds learning into stabilized Petrov–Galerkin formulations by learning stabilization parameters or residual-based terms that are naturally expressed at the element/weak level [Tassi et al., 2023]. Parallel threads train models by minimizing weak residuals to target weak solutions more directly [Zang et al., 2020, Chen et al., 2023, De Ryck et al., 2024].

We present a weak-form correction approach for hybrid physics–ML modeling on coarse grids for an incompressible finite element solver. We augment the momentum equation with parameterized bilinear contributions whose coefficients are trained from high-resolution solutions projected onto coarse grids. Learning in the weak form couples the correction to the PDE operator, enabling structure-preserving designs that respect numerical stability in a finite element solver. We demonstrate the approach on two test cases: the 1D convection–diffusion equation and the 2D Navier–Stokes equations.

The remainder of this paper is organized as follows. Section 2 describes the simulation setup in Firedrake and the datasets used. Section 3 details the methodology and the end-to-end training implementation in Firedrake. Section 4 presents results for the 1D convection–diffusion equation and 2D flow past a cylinder. Section 5 concludes with a summary and directions for future work.

2 Simulation and datasets

This section outlines the simulation settings and datasets used in our study. We consider two examples: the one-dimensional convection–diffusion equation and the two-dimensional incompressible Navier–Stokes equations for flow past a cylinder.

2.1 Simulation

We use the finite-element-based Firedrake [Ham et al., 2023] framework built on PETSc [Balay et al., 2019] to formulate both problems in weak form and to solve the linear and nonlinear systems using PETSc’s SNES/KSP solvers with appropriate preconditioning for the linearized subproblems. We couple Firedrake with PyTorch and employ differentiable programming tools that provide end-to-end derivatives of simulation-based objectives with respect to physical parameters, initial/boundary conditions, and learnable closures. Time-dependent cases are advanced with a Crank–Nicolson (CN) scheme. At each step, we solve the discrete residual to a fixed tolerance and record the fields required to construct the training/test datasets described below.

2.2 One-dimensional convection–diffusion equation

We first study the propagation of a multi-frequency initial signal governed by the 1D convection–diffusion equation:

$$\frac{\partial u}{\partial t} + a \frac{\partial u}{\partial x} = \nu \frac{\partial^2 u}{\partial x^2}, \quad x \in [0, 1], \quad t \in [0, T], \quad (2.1)$$

where $u(x, t)$ denotes the scalar field, a is the convection coefficient, and ν is the diffusion coefficient. In all tests we fix $a = 1$ and $\nu = 0.0001$ in Eq. (2.1), and we impose periodic boundary conditions at $x = 0$ and $x = 1$. The initial condition is prescribed as

$$u(t = 0, x) = 4 \sum_{i=1}^4 \sin(2\pi\alpha_i(x - \phi)), \quad (2.2)$$

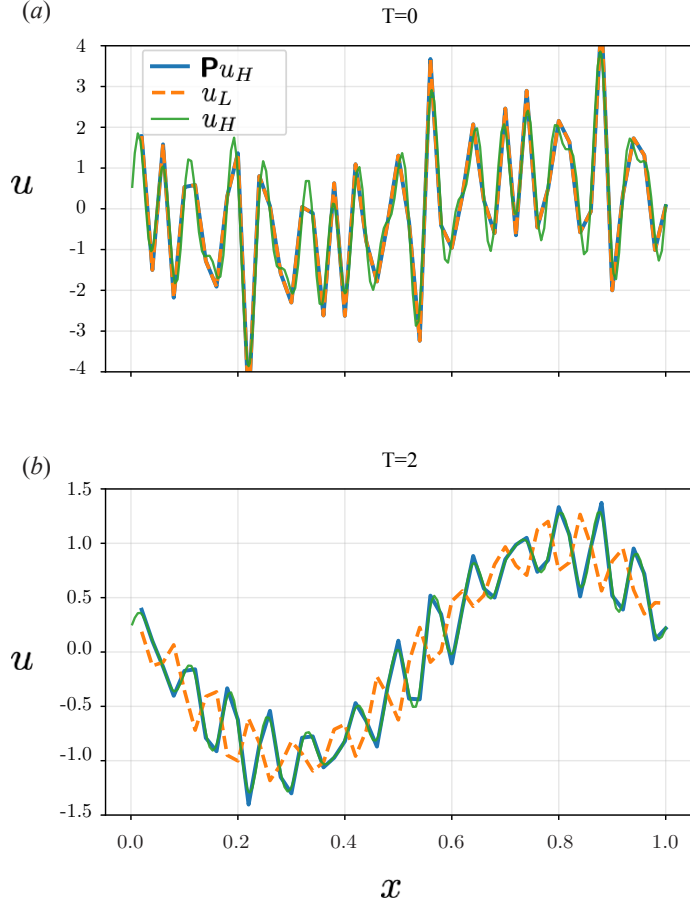


FIGURE 1: 1D CONVECTION-DIFFUSION EQUATION: (a) INITIAL CONDITION AND (b) SOLUTION AT $T = 2$.

with $\alpha_i = \{4, 6, 7, 20\}$ and a phase shift $\phi \sim \mathcal{U}(0, 1)$, as shown in Figure 1(a). For each sampled ϕ , Eq. (2.1) is advanced in time by using a CN scheme. To generate reference data, we run simulations for 100 randomly sampled phases ϕ over $t \in [0, 2]$ on a mesh of 50 elements using a high-order continuous Galerkin discretization in Firedrake. The last step solution at $T = 2$ is shown in Figure 1(b). The resulting spatiotemporal high-fidelity solutions are denoted by u_H ($P = 5$), yielding 250 degrees of freedom (DOFs), and are shown in Figure 2(a). The coarse field is computed via the $L_2(\Omega)$ (Galerkin) projection of the high-resolution solution $u_H \in V_H$ onto the low-resolution space V_L . Specifically, $Pu_H \in V_L$ is defined by

$$(Pu_H, v)_{L_2(\Omega)} = (u_H, v)_{L_2(\Omega)} \quad \forall v \in V_L, \quad (2.3)$$

where the $L_2(\Omega)$ inner product is $(a, b)_{L_2(\Omega)} := \int_{\Omega} a(x) b(x) dx$. The coarse field Pu_H is shown in Figure 2(b). These projected fields are used to construct the training and test datasets. We use the projected trajectory Pu_H as the learning target. Training data span $t \in [0, 2]$, and testing uses a separate $t \in [0, 5]$ segment with a different phase. This phase-shifted test set is then used to assess longer-horizon predictive performance. For comparison, the corresponding low-resolution simulation ($P = 1$) is shown in Figure 2(c).

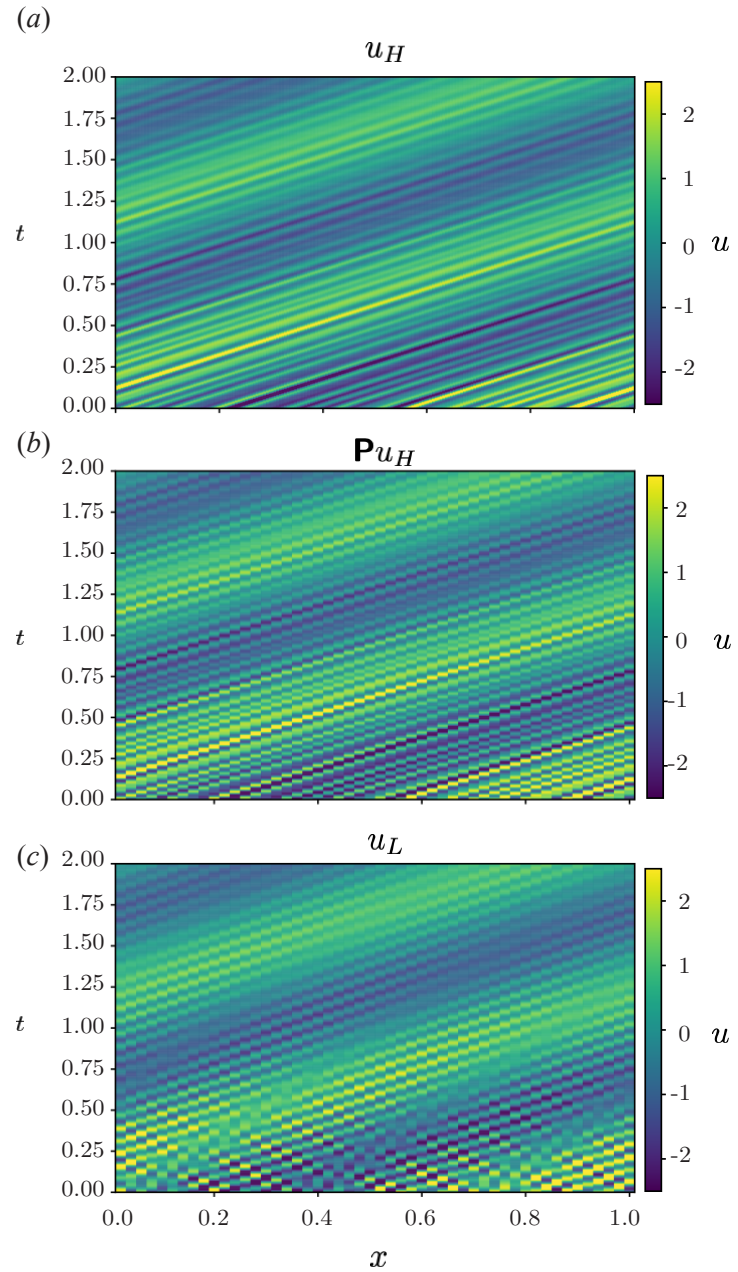


FIGURE 2: SPACE-TIME FIELDS FOR THE 1D CONVECTION-DIFFUSION EQUATION. (a) HIGH-RESOLUTION SOLUTION u_H . (b) PROJECTED FIELD $\mathbf{P}u_H$. (c) LOW-RESOLUTION SOLUTION u_L .

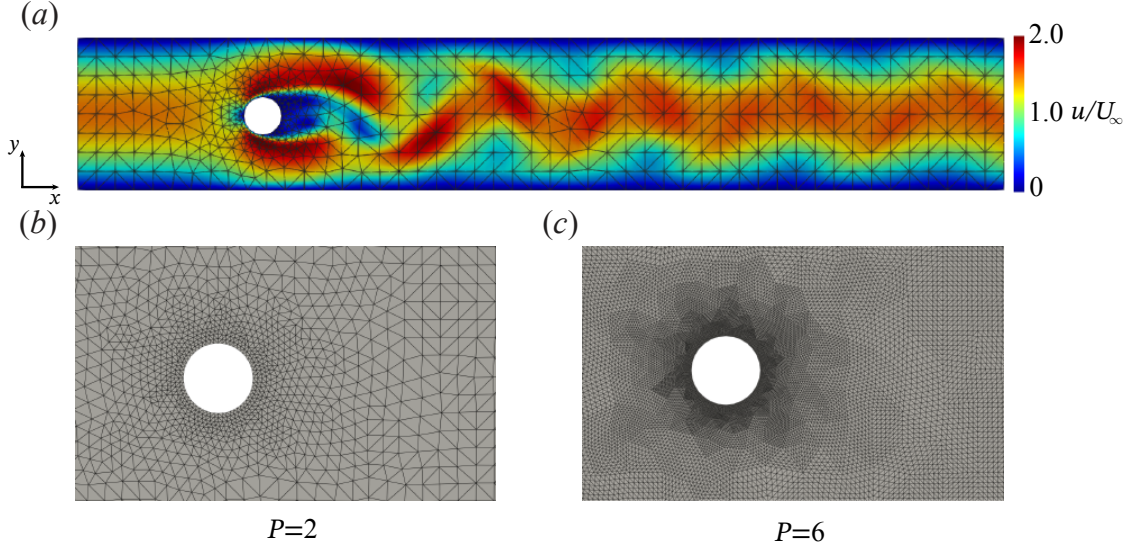


FIGURE 3: 2D FLOW PAST A CYLINDER: (a) COMPUTATIONAL MESH COLORED BY THE INSTANTANEOUS VELOCITY MAGNITUDE (ONLY ELEMENT EDGES ARE SHOWN). (b) HIGH-RESOLUTION GRID ($p_v, p_p = 6, 5$) WITH ZOOMED-IN MESH INSETS NEAR THE CYLINDER. (c) LOW-RESOLUTION GRID ($p_v, p_p = 2, 1$).

2.3 Two-dimensional flow past a cylinder

We simulate two-dimensional flow past a circular cylinder in a channel at Reynolds number 100 using Firedrake [Ham et al., 2023] on the standard benchmark geometry [Schäfer et al., 1996]. The incompressible Navier–Stokes equations on a bounded domain $\Omega \subset \mathbb{R}^2$ with boundary $\partial\Omega$ over $t \in (0, T]$ are

$$\begin{aligned} \partial_t \mathbf{u} + (\mathbf{u} \cdot \nabla) \mathbf{u} + \nabla p - \nu \Delta \mathbf{u} &= 0 & \text{in } \Omega, \\ \nabla \cdot \mathbf{u} &= 0 & \text{in } \Omega. \end{aligned} \quad (2.4)$$

We adopt the standard spaces $V = [H^1(\Omega)]^2$ and $Q = L^2(\Omega)$, with finite-dimensional subspaces $V_h \subset V$ and $Q_h \subset Q$. Eq. (2.4) is solved with no-slip conditions on the cylinder and channel walls, a laminar parabolic inflow at Γ_I ,

$$u_{\text{in}}(y) = \frac{4V_{\text{max}} y(0.41 - y)}{0.41^2}, \quad v_{\text{in}}(y) = 0 \quad (V_{\text{max}} = 1.5),$$

and a traction-free outflow at Γ_O . Baseline parameters are $\nu = 0.001$, $\Delta t = 0.01$, $T_0 = 0$, and $T_{\text{end}} = 53$. The training set spans $300 \Delta t$, and the test set spans $5000 \Delta t$. The computational domain is $\Omega = [0, 2.5] \times [0, 0.41]$ with a circular cylinder of radius 0.05 embedded in the channel, shown in Figure 3. We discretize in space using inf–sup–stable Taylor–Hood elements. For the high-fidelity reference solution, we employ polynomial degrees $(p_v, p_p) = (6, 5)$, resulting in 40,884 velocity DOFs and 14,255 pressure DOFs. For the coarse-resolution runs we use $(2, 1)$, which yields 4,732 velocity DOFs and 627 pressure DOFs. Time integration is performed with a CN scheme at each time step.

3 Methodology

We begin by briefly reviewing strong-form correction strategies used in prior work [De Lara and Ferrer, 2022, Kang and Constantinescu, 2023, Otmani et al., 2025, Kang and Constantinescu, 2025, Jung and Constantinescu, 2025]. Next, we motivate a weak-form perspective using the two-dimensional incompressible

Navier–Stokes equations as a representative example. Then, we present the proposed weak-form correction approach. Finally, we describe the training objective and the differentiable learning pipeline, which combines discrete adjoints in the Firedrake solver with backpropagation implemented in PyTorch.

3.1 Strong-form correction

In general, a strong-form correction augments the governing equation as

$$\frac{\partial \mathbf{u}}{\partial t} = \mathcal{F}(\mathbf{u}(t)) + \mathcal{N}_\theta(\mathbf{u}), \quad (3.1)$$

where \mathcal{F} denotes the nonlinear operator defining the resolved dynamics. The term $\mathcal{N}_\theta(\mathbf{u})$ is a learned neural operator that acts as an additional source to account for unresolved (subgrid) effects on a coarse grid. In this setting, training is performed through the time-integration procedure, which requires a differentiable solver to enable multistep, unsupervised learning.

In a finite element formulation, this correction appears in the weak form as the pointwise forcing term $(\mathcal{N}_\theta(\mathbf{u}), \mathbf{v})$. This contrasts with approaches based on bilinear-form (operator) corrections, which modify the discrete operator itself rather than adding an explicit source.

3.2 Weak-form correction

The semi-discrete Galerkin formulation of the incompressible Navier–Stokes equations seeks $(\mathbf{u}_h(t), p_h(t)) \in V_h \times Q_h$ such that for all $(\mathbf{v}_h, q_h) \in V_h \times Q_h$ and $t \in (0, T]$,

$$\begin{aligned} (\partial_t \mathbf{u}_h, \mathbf{v}_h)_\Omega + \nu (\nabla \mathbf{u}_h, \nabla \mathbf{v}_h)_\Omega + c_{\text{skew}}(\mathbf{u}_{\text{adv}}, \mathbf{u}_h, \mathbf{v}_h) \\ - (p_h, \nabla \cdot \mathbf{v}_h)_\Omega + (q_h, \nabla \cdot \mathbf{u}_h)_\Omega = 0. \end{aligned} \quad (3.2)$$

Here, \mathbf{u}_{adv} denotes the advecting velocity (e.g., \mathbf{u}_h for the fully nonlinear form or a lagged/extrapolated field in linearized Oseen-type updates). We adopt the skew-symmetric convection operator

$$c_{\text{skew}}(\mathbf{a}; \mathbf{w}, \mathbf{v}) = \frac{1}{2} \left((\mathbf{a} \cdot \nabla \mathbf{w}, \mathbf{v})_\Omega - (\mathbf{a} \cdot \nabla \mathbf{v}, \mathbf{w})_\Omega \right). \quad (3.3)$$

This form is skew-adjoint and therefore satisfies $c_{\text{skew}}(\mathbf{a}; \mathbf{w}, \mathbf{w}) = 0$ for any \mathbf{a} , which prevents artificial kinetic energy production from the discrete convection term.

To obtain a stable and physically interpretable correction mechanism within the finite element weak setting, we introduce three scalar coefficient fields $c_{\text{adv}}(\mathbf{u}_h)$, $\nu_t(\mathbf{u}_h)$, and $\gamma(\mathbf{u}_h)$. Each coefficient is represented in a low-order scalar finite element space S_h , so that $c_{\text{adv}}(\mathbf{u}_h), \nu_t(\mathbf{u}_h), \gamma(\mathbf{u}_h) \in S_h$ and, in the discrete implementation, each field is encoded by a vector of $N_{\text{coef}} = \dim(S_h)$ DOFs. We constrain the coefficients to lie in the bounds $c_{\text{adv}}(\mathbf{u}_h) \in [-c_{\text{max}}, c_{\text{max}}]$, $\nu_t(\mathbf{u}_h) \in [0, \nu_{t,\text{max}}]$, and $\gamma(\mathbf{u}_h) \in [0, \gamma_{\text{max}}]$, which modulate the strength of advection (c_{adv}), augment diffusion through an eddy viscosity (ν_t), and provide grad-div stabilization (γ), respectively. The corrected semi-discrete problem consists in determining $(\mathbf{u}_h(t), p_h(t)) \in V_h \times Q_h$ such that for all $(\mathbf{v}_h, q_h) \in V_h \times Q_h$,

$$\begin{aligned} (\partial_t \mathbf{u}_h, \mathbf{v}_h)_\Omega + ((\nu + \nu_t) \nabla \mathbf{u}_h, \nabla \mathbf{v}_h)_\Omega \\ + (1 + c_{\text{adv}}) c_{\text{skew}}(\mathbf{u}_{\text{adv}}, \mathbf{u}_h, \mathbf{v}_h) \\ - (p_h, \nabla \cdot \mathbf{v}_h)_\Omega + (q_h, \nabla \cdot \mathbf{u}_h)_\Omega \\ + (\gamma \nabla \cdot \mathbf{u}_h, \nabla \cdot \mathbf{v}_h)_\Omega + \varepsilon_p (p_h, q_h)_\Omega = 0. \end{aligned} \quad (3.4)$$

The small parameter $\varepsilon_p \geq 0$ is an optional pressure penalty used solely to regularize the mixed linear algebra for certain solver configurations. The corrections enter through bilinear forms assembled in the same finite element framework, which preserves sparsity and locality, maintains compatibility with existing solvers and preconditioners, and supports discrete-adjoint consistency.

Algorithm 1 End-to-end training of weak-form correction (rollout length m)

Input: snapshots $\{\mathbf{u}^n\}_{n=0}^T$, timestep Δt , rollout m , model \mathcal{N}_θ

repeat

Sample mini-batch B of restart indices s_0 ; **zero grads**

for $s_0 \in B$ **do**

$\mathbf{u} \leftarrow \mathbf{u}^{s_0}$; $J \leftarrow 0$

for $j = 0$ **to** $m - 1$ **do**

$\boldsymbol{\eta}_{s_0+j} \leftarrow \mathcal{N}_\theta(\text{vec}(\mathbf{u}))$

$\tilde{\mathbf{u}} \leftarrow \text{solve (3.4) with } \boldsymbol{\eta}_{s_0+j}$

$J \leftarrow J + \frac{1}{2} \|\tilde{\mathbf{u}} - \mathbf{u}^{s_0+j+1}\|_{L^2}^2$

$\mathbf{u} \leftarrow \tilde{\mathbf{u}}$

$\left\{ \frac{dJ}{d\boldsymbol{\eta}_{s_0+j}} \right\}_{j=0}^{m-1} \leftarrow \text{discrete adjoint of taped rollout (Firedrake adjoint)}$

Backpropagate on each $\boldsymbol{\eta}_{s_0+j}$ with $\frac{d\boldsymbol{\eta}_{s_0+j}}{d\theta}$ (PyTorch)

until converged

Return: trained parameters θ^*

3.3 Training objective and end-to-end training via discrete adjoints and backpropagation

We define the training objective and summarize the learning algorithm. Given snapshot data $\{\mathbf{u}^n\}$, we define the per-step mismatch functional

$$J^{n+1}(\theta) = \frac{1}{2} \int_{\Omega} \left\| \tilde{\mathbf{u}}_{h,\theta}^{n+1} - \mathbf{u}^{n+1} \right\|^2 d\Omega, \quad (3.5)$$

where $\tilde{\mathbf{u}}_{h,\theta}^{n+1}$ is the one-step prediction produced by the corrected solver. Training uses random restart indices s_0 and rollouts of length m time steps. For each rollout and each substep $j = 0, \dots, m - 1$, we construct correction fields from the current state $\mathbf{u}_h^{s_0+j}$, advance the corrected weak form (3.4) to obtain $\tilde{\mathbf{u}}_{h,\theta}^{s_0+j+1}$, and evaluate (3.5) against \mathbf{u}^{s_0+j+1} . The total rollout objective is

$$J(\theta) = \sum_{j=0}^{m-1} J^{s_0+j+1}(\theta), \quad (3.6)$$

and we differentiate J through the entire m -step time-marching map. Algorithm 1 summarizes the procedure.

We compute discrete sensitivities of the rollout objective with respect to the correction fields using algorithmic differentiation of the finite element solver (Firedrake adjoint). In particular, for each substep we obtain $\frac{dJ}{dc_{\text{adv}}}$, $\frac{dJ}{d\nu_t}$, and $\frac{dJ}{d\gamma}$ in the coefficient dual space S_h^* . These adjoint sensitivities provide upstream gradients for the neural parameterization, and the chain rule gives

$$\frac{dJ}{d\theta} = \sum_{j=0}^{m-1} \underbrace{\left(\frac{\partial \boldsymbol{\eta}_{s_0+j}}{\partial \theta} \right)^\top}_{\text{PyTorch}} \underbrace{\frac{dJ}{d\boldsymbol{\eta}_{s_0+j}}}_{\text{Firedrake adjoint}}, \quad (3.7)$$

where $\boldsymbol{\eta}$ denotes the learned coefficient fields for $(c_{\text{adv}}, \nu_t, \gamma)$.

In implementation, we couple solver-adjoint gradients to PyTorch by seeding backpropagation on the coefficient tensors with the adjoint-derived sensitivities. Parameters are updated with Adam. Gradient clipping and learning-rate scheduling are applied to improve robustness.

4 Results

This section reports results for two test cases that demonstrate the proposed weak-form correction approach. For each example, we compare weak-form and strong-form corrections in terms of (i) training performance

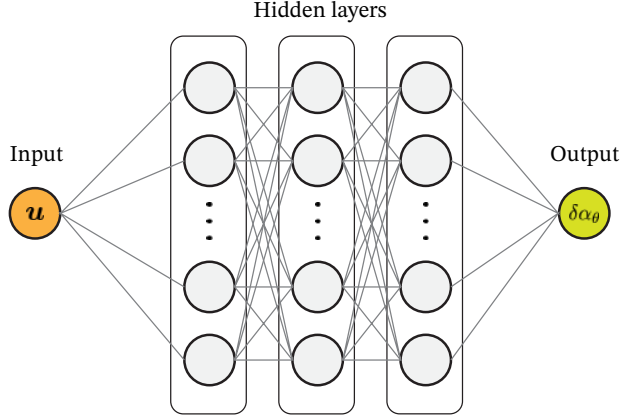


FIGURE 4: ARCHITECTURE OF CORRECTIVE OPERATOR FOR 1D CONVECTION-DIFFUSION EQUATION.

(loss history), (ii) predictive accuracy relative to the projected high-resolution reference solution, and (iii) computational efficiency, quantified by speedup relative to the high-resolution solver and by time-averaged error over long rollouts, in other words, the effective prediction horizon. All experiments were run on an Apple Silicon Mac (M4) using PyTorch’s MPS GPU backend.

4.1 One-dimensional convection-diffusion equation

We start from a semi-discrete weak formulation on the coarse finite element space and introduce neural corrections directly at the variational level. In the experiments reported here, we employ a bilinear weak-form correction. That is, we learn a correction field that enters through the term paired with the test-function derivative,

$$\delta\alpha_\theta = \mathcal{N}_\theta(\mathbf{u}_h), \quad (4.1)$$

where \mathcal{N}_θ is a neural network evaluated on the nodal degree of freedom vector of the coarse solution \mathbf{u}_h . The corrected weak formulation seeks $\mathbf{u}_h(t) \in V_h$ such that, for all $\mathbf{v}_h \in V_h$ and $t \in (0, T]$,

$$(\partial_t \mathbf{u}_h, \mathbf{v}_h)_\Omega + (a \mathbf{u}_{h,x}, \mathbf{v}_h)_\Omega + (\nu \mathbf{u}_{h,x}, \mathbf{v}_{h,x})_\Omega + (\delta\alpha_\theta, \mathbf{v}_{h,x})_\Omega = 0. \quad (4.2)$$

Here $(\delta\alpha_\theta, \mathbf{v}_{h,x})_\Omega$ acts as a learned correction to the resolved transport-diffusion balance through a weak flux-like contribution. Since periodic boundary conditions are imposed at $x = 0$ and $x = 1$, no boundary integrals arise in Eq. (4.2). When the baseline coarse model is sufficient, training drives $\delta\alpha_\theta \approx 0$, recovering the standard Galerkin method.

For training, we minimize a multistep rollout loss over a horizon of length $m = 20$. Mini-batches are constructed by randomly sampling short subsequences from the stored projected reference trajectories $\mathbf{P}\mathbf{u}_H$. For each sampled subsequence, the model is rolled out for m steps, and the parameters are updated by minimizing the mean-squared error between the predicted rollout and the reference subsequence over the full horizon. Time integration during both training and evaluation is performed using a CN scheme. The correction field $\delta\alpha_\theta$ is parameterized by a multilayer perceptron with three ReLU-activated hidden layers of widths (128, 128, 128), as shown in Figure 4. We train for 1,000 epochs with batch size $B = 10$ and 10 batches per epoch. The learning rate is initialized at 10^{-3} and decayed multiplicatively by a factor of 0.99 per epoch. Both the strong-form and weak-form models are trained on the same dataset using the same rollout loss. They use identical network architectures with the same number of parameters. The only difference is where the learned correction is applied, either as a strong-form term or as a weak-form

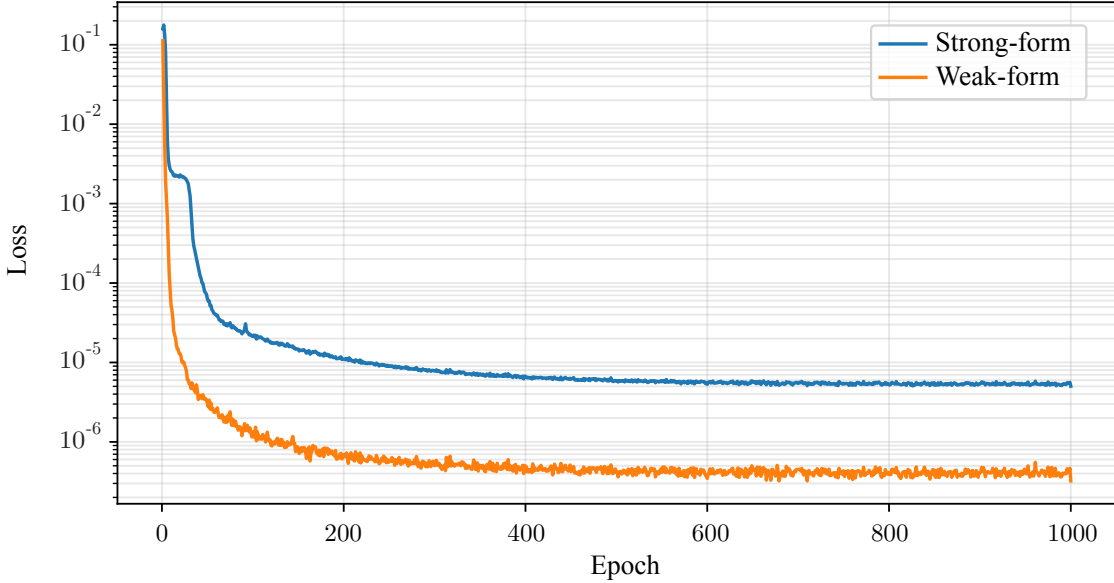


FIGURE 5: TRAINING LOSS VERSUS EPOCH FOR STRONG-FORM AND WEAK-FORM CORRECTIONS IN 1D CONVECTION-DIFFUSION EQUATION.

variational contribution.

As shown in Figure 5, the training loss decreases rapidly in the initial epochs and then gradually levels off. Small fluctuations in the loss are expected due to random mini-batch sampling. Over the full training window, the weak-form model consistently achieves a lower loss than the strong-form model, consistent with weak-form correction providing a numerically structure-preserving formulation that is less sensitive to pointwise high-frequency residuals.

Figure 6 evaluates long-horizon rollout accuracy using the normalized relative error

$$e(t) = \frac{\|\tilde{u}(t) - \mathbf{P}u_H(t)\|_2}{\|\mathbf{P}u_H(t)\|_2}, \quad (4.3)$$

where \tilde{u} denotes the model prediction and $\mathbf{P}u_H$ is the projected reference trajectory on the coarse space. Across the full rollout interval ($t \in [0, 5000\Delta t]$), the weak-form correction achieves a lower relative error than does the strong-form correction. Moreover, the weak-form model exhibits a slower growth rate of $e(t)$, particularly at later times, indicating improved robustness under iterative time stepping when error accumulation typically becomes dominant. In contrast, the strong-form correction shows a larger drift and faster error growth, reflecting reduced stability in long-horizon prediction. The space-time relative-error maps in Figure 7 further clarify these trends. The strong-form correction produces higher error magnitudes with localized, persistent error bands that propagate in time, suggesting that pointwise (strong-form) forcing corrections do not sufficiently constrain the evolving solution under repeated rollout. The weak-form correction yields a more uniformly bounded error field, with reduced peak values and fewer localized artifacts, consistent with improved numerical stability of the learned correction. Overall, the temporal error curves (Figure 6) and space-time diagnostics (Figure 7) indicate that weak-form correction is better aligned with the discretized convection-diffusion dynamics and delivers more robust improvements in multistep forecasting.

Table 1 reports the time-averaged relative L^2 rollout error, $\bar{\varepsilon}_{L^2}$, along with the computational speedup relative to the high-resolution solver. The metric is defined as $\bar{\varepsilon}_{L^2} = \frac{1}{T} \int_0^T e(t) dt$. The low-resolution baseline (u_L) is faster than the high-resolution solver (18.9 \times) but exhibits substantial accumulated error.

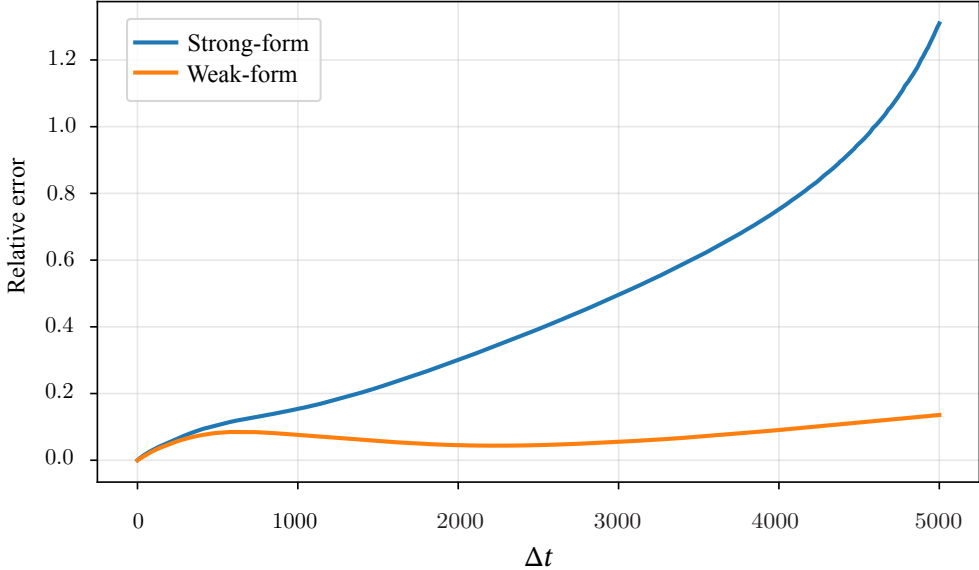


FIGURE 6: TIME EVOLUTION OF THE RELATIVE ROLLOUT ERROR FOR THE 1D CONVECTION-DIFFUSION EQUATION USING STRONG-FORM AND WEAK-FORM NEURAL CORRECTIVE OPERATORS.

TABLE 1: TIME-AVERAGED RELATIVE L^2 ERROR OVER THE ROLLOUT INTERVAL $t \in [0, 5000\Delta t]$ AND COMPUTATIONAL COST RELATIVE TO THE HIGH-RESOLUTION SOLVER.

Method	$\bar{\varepsilon}_{L^2}$	Speedup (\times)
High-resolution reference (u_H)	0.0	1.0
Low-resolution baseline (u_L)	1.5	18.9
Strong-form correction	4.60×10^{-1}	17.6
Weak-form correction	7.14×10^{-2}	17.5

Both correction strategies substantially improve accuracy while also maintaining similar speedups. The strong-form correction reduces the rollout error to 4.60×10^{-1} , corresponding to a $3.26\times$ reduction in error relative to u_L , and achieves a $17.6\times$ speedup. The weak-form correction further lowers the error to 7.14×10^{-2} (an additional $6.4\times$ reduction in error relative to the strong-form correction and $21\times$ relative to u_L , while maintaining a similar speedup $17.5\times$). Overall, the weak-form correction provides the best accuracy, delivering the lowest time-averaged rollout error at essentially the same runtime as the strong-form approach.

4.2 Two-dimensional flow past a cylinder

Following Section 3.2, we train the learned corrective operators using a CN Oseen-type weak form. Let $\delta_t \mathbf{u}_h^{n+1} := (\mathbf{u}_h^{n+1} - \mathbf{u}_h^n)/\Delta t$ with $\Delta t = 10^{-2}$ and $\theta_{CN} = 0.5$. We seek $(\mathbf{u}_h^{n+1}, p_h^{n+1}) \in V_h \times Q_h$ such that, for all $(\mathbf{v}, q) \in V_h \times Q_h$,

$$\begin{aligned}
 & (\delta_t \mathbf{u}_h^{n+1}, \mathbf{v})_\Omega + \theta_{CN} \mathcal{A}(\mathbf{u}_h^{n+1}, p_h^{n+1}; \mathbf{v}, q) \\
 & + (1 - \theta_{CN}) \mathcal{A}(\mathbf{u}_h^n, p_h^n; \mathbf{v}, q) = 0.
 \end{aligned} \tag{4.4}$$

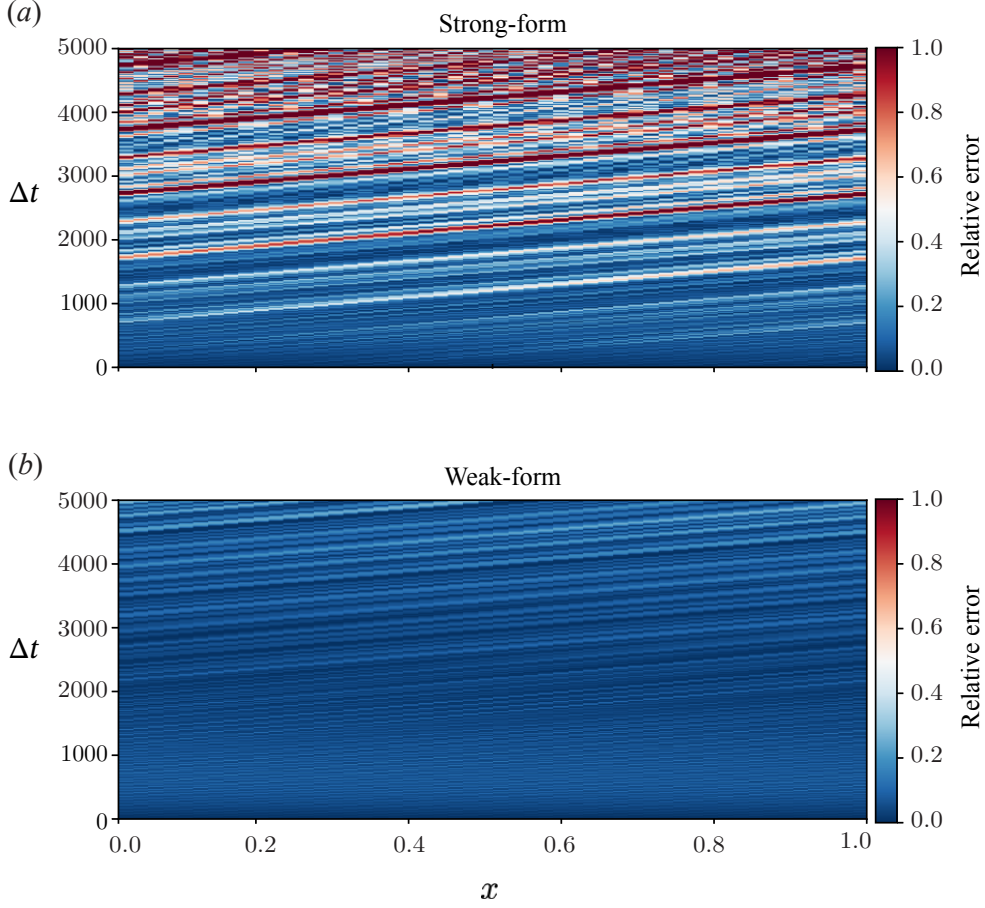


FIGURE 7: RELATIVE ERROR FIELDS IN SPACE-TIME FOR THE 1D CONVECTION-DIFFUSION EQUATION, COMPARING (a) STRONG-FORM AND (b) WEAK-FORM CORRECTIVE OPERATORS.

The Oseen operator is

$$\begin{aligned} \mathcal{A}(\mathbf{u}, p; \mathbf{v}, q) = & ((\nu + \nu_t) \nabla \mathbf{u}, \nabla \mathbf{v})_{\Omega} \\ & + (1 + c_{\text{adv}}) c_{\text{skew}}(\mathbf{u}_{\text{adv}}^n; \mathbf{u}, \mathbf{v}) \\ & - (p, \nabla \cdot \mathbf{v})_{\Omega} + (q, \nabla \cdot \mathbf{u})_{\Omega} \\ & + (\gamma \nabla \cdot \mathbf{u}, \nabla \cdot \mathbf{v})_{\Omega} + \varepsilon_p (p, q)_{\Omega}. \end{aligned} \quad (4.5)$$

We use $\nu = 10^{-3}$ and a small pressure regularization $\varepsilon_p = 10^{-10}$ for numerical stability.

We learn three corrective coefficient fields (c_{adv} , ν_t , γ), introduced in Section 3.2. At each CN step, these fields are predicted by a neural network from the current velocity state,

$$(c_{\text{adv}}, \nu_t, \gamma) = \mathcal{N}_{\theta}(\mathbf{u}_h). \quad (4.6)$$

The learned corrective fields are discretized in a lower-order finite element space with $N_{\text{coef}} = 4732$ DOFs for $P = 2$ and two velocity components. The neural network takes as input the current velocity field represented in the same scalar space and outputs the three coefficient fields (c_{adv} , ν_t , γ), giving an output dimension of $3N_{\text{coef}}$. We train by minimizing a multistep rollout loss over $m = 20$ time steps. The dataset spans the time interval $t \in [0, 53]$, including $300\Delta t$ for training and $5000\Delta t$ for testing. Training is performed for 500 epochs with mini-batch size $B = 10$. Optimization uses Adam with an initial learning rate 10^{-4} and an exponential schedule per epoch, with a minimum learning rate of 10^{-6} . The corrective operator \mathcal{N}_{θ} is implemented as a

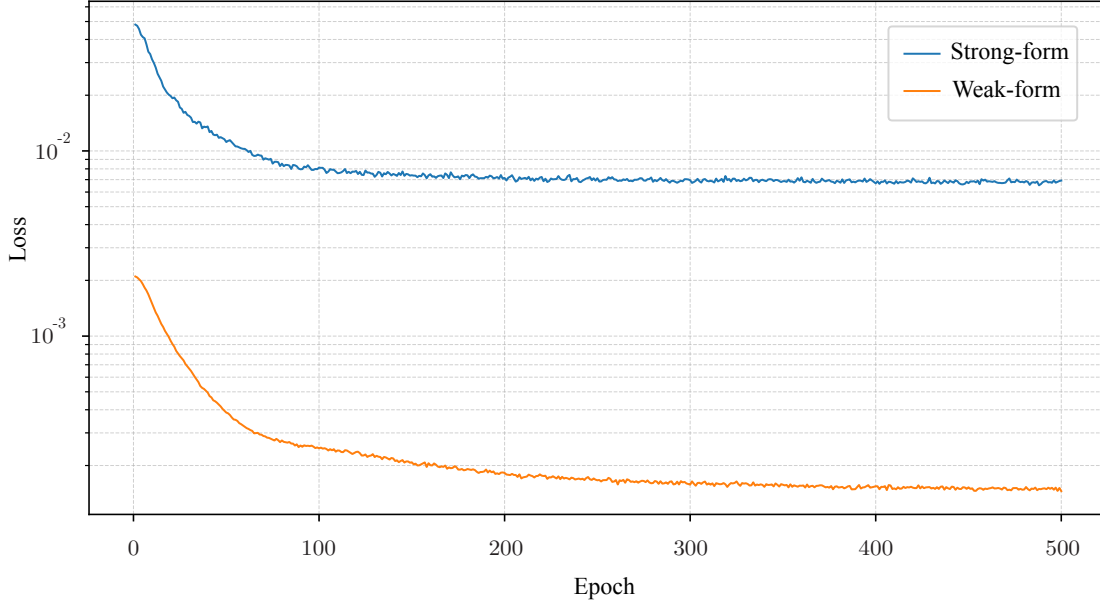


FIGURE 8: TRAINING LOSS VERSUS EPOCH FOR THE STRONG-FORM AND WEAK-FORM CORRECTIONS APPLIED TO 2D FLOW PAST A CYLINDER.

fully connected multilayer perceptron with three hidden layers of widths (5000, 4000, 3000).

The training loss histories for the strong-form and weak-form corrections are compared in Figure 8. Both approaches display a typical two-stage optimization trend, with a sharp reduction over the first 100 epochs followed by a slower, asymptotic decay. Importantly, the weak-form correction maintains a substantially lower loss throughout training. It starts at $\mathcal{O}(10^{-3})$, drops rapidly during the early stage, and continues to decrease gradually to $\mathcal{O}(10^{-4})$ by 500 epochs. In contrast, the strong-form loss begins at $\mathcal{O}(10^{-2})$ and plateaus near $\sim 7 \times 10^{-3}$ after the initial decay, showing only small fluctuations thereafter. Overall, Figure 8 indicates that weak-form training reaches a markedly lower terminal value (roughly 40–50× lower than the strong-form case). From a numerical perspective, this behavior is consistent with the weak-form formulation providing a better-conditioned enforcement of the governing constraints via integral residuals, which are less sensitive to localized high-frequency discrepancies and can yield smoother, more stable optimization dynamics.

Figure 9 shows the rollout relative error of Eq. (4.3) as a function of time step (Δt), which we use to evaluate the trained model for corrected dynamical simulations. The baseline low-fidelity solution u_L exhibits pronounced, periodic errors of $\mathcal{O}(10^{-1})$, indicating phase and amplitude mismatches and the accumulation of time-integration error in the vortex-shedding regime. This behavior is also visible in the second-row (u_L) of snapshots in Figures 10 and 11. Both corrected models reduce the short-term error relative to \tilde{u}_L , as shown in the second-row (strong-form) and third-row (weak-form) results in Figure 11. However, their long-horizon behavior differs substantially, as illustrated in Figure 11(b)–(d).

Table 2 reports the time-averaged relative L^2 error for both short- ($t \in [0, 1000\Delta t]$) and long-horizon ($t \in [0, 5000\Delta t]$) rollouts, along with the associated computational cost. The low-resolution baseline u_L exhibits a large mean error $\mathcal{O}(10^{-1})$ on both time intervals. Both correction strategies markedly reduce the short-horizon error on $t \in [0, 1000\Delta t]$. The strong-form correction decreases $\bar{\varepsilon}_{L^2}$ from 3.07×10^{-1} to 7.78×10^{-2} (about 4× improvement) with essentially unchanged computational cost (158× speedup). The weak-form correction yields the best short-term performance, achieving 2.73×10^{-2} (about 11× improvement over u_L) while retaining a comparable speedup (156×). Over the longer horizon $t \in [0, 5000\Delta t]$, the two

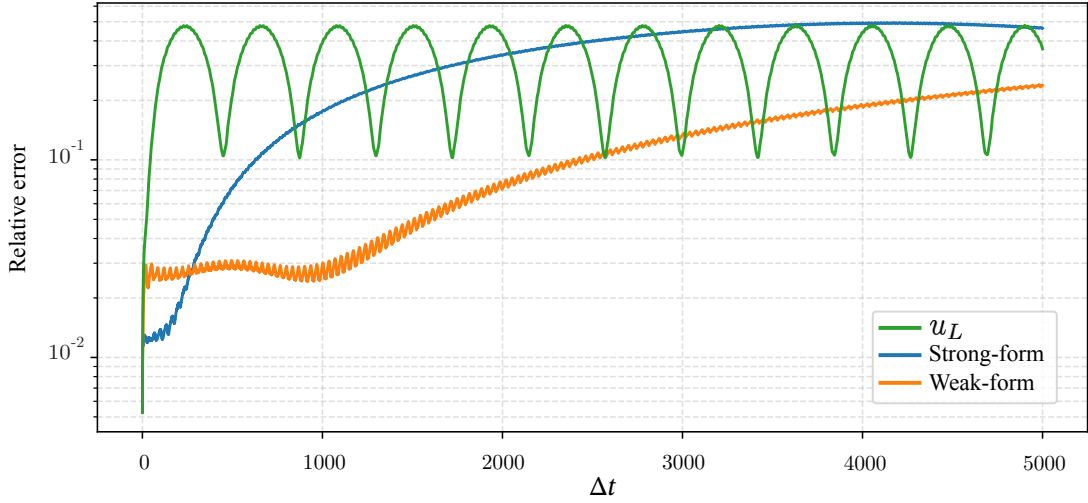


FIGURE 9: TIME EVOLUTION OF THE RELATIVE ROLLOUT ERROR FOR THE 2D FLOW PAST A CYLINDER USING STRONG-FORM AND WEAK-FORM NEURAL CORRECTIVE OPERATORS.

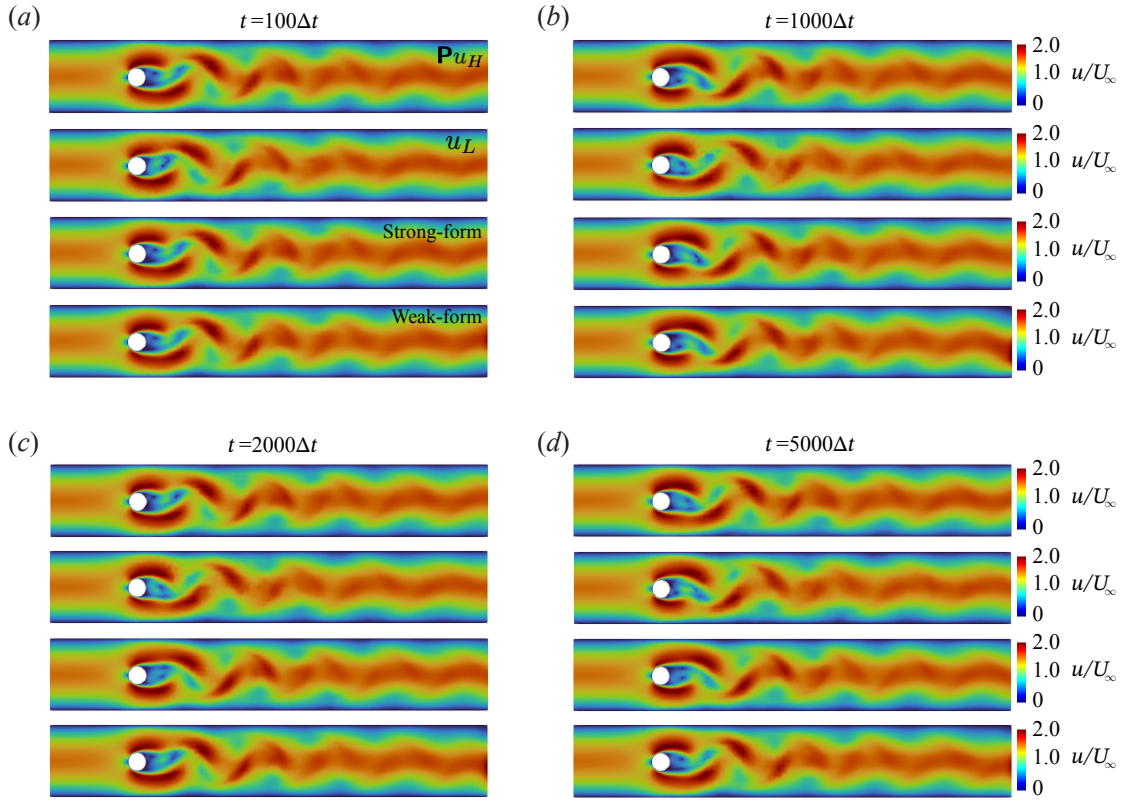


FIGURE 10: SNAPSHOTs OF ROLLOUT PREDICTIONS AT $t = [100\Delta t, 1000\Delta t, 2000\Delta t, 5000\Delta t]$ USING STRONG-FORM AND WEAK-FORM NEURAL CORRECTIVE OPERATORS.

corrected models separate more clearly. The strong-form correction loses its advantage and degrades to 3.39×10^{-1} , slightly worse than the baseline, suggesting error accumulation and reduced long-term stability.

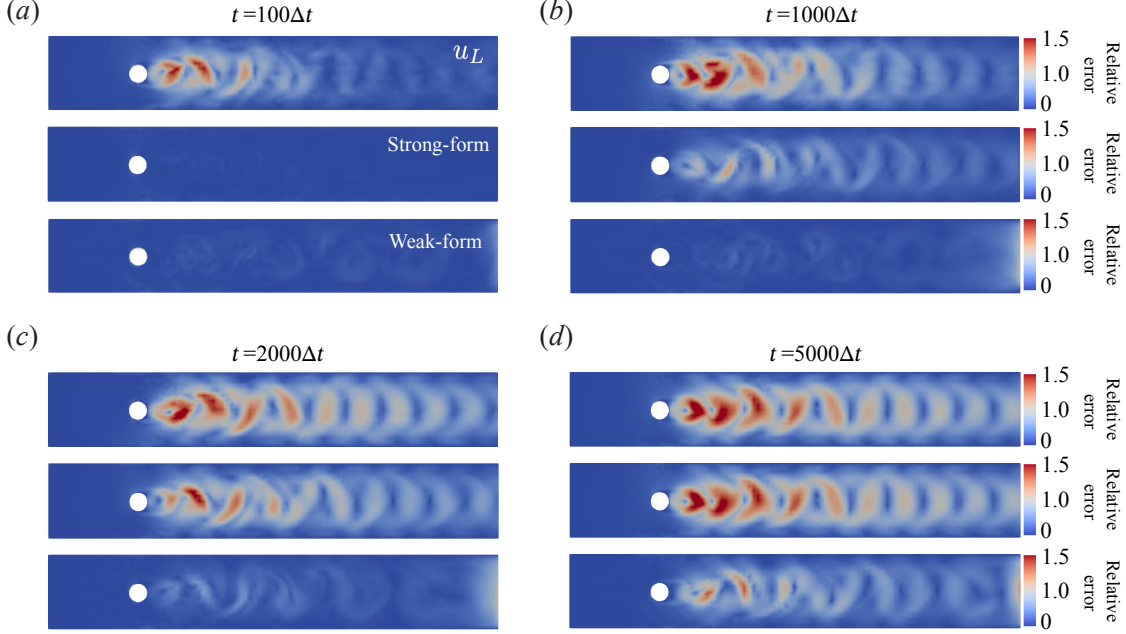


FIGURE 11: SNAPSHOTS OF ROLLOUT RELATIVE ERRORS AT $t = [100\Delta t, 1000\Delta t, 2000\Delta t, 5000\Delta t]$ USING STRONG-FORM AND WEAK-FORM NEURAL CORRECTIVE OPERATORS.

TABLE 2: TIME-AVERAGED RELATIVE L^2 ERROR OVER THE ROLLOUT INTERVALS $t \in [0, 1000\Delta t]$ AND $t \in [0, 5000\Delta t]$ AND COMPUTATIONAL COST RELATIVE TO THE HIGH-RESOLUTION SOLVER.

Method	$\bar{\varepsilon}_{L^2} [0, 1000\Delta t]$	$\bar{\varepsilon}_{L^2} [0, 5000\Delta t]$	Speedup (\times)
High-resolution reference (u_H)	0	0	1
Low-resolution baseline (u_L)	3.07×10^{-1}	3.27×10^{-1}	169
Strong-form correction	7.78×10^{-2}	3.39×10^{-1}	158
Weak-form correction	2.73×10^{-2}	1.10×10^{-1}	156

In contrast, the weak-form correction maintains a substantially lower mean error 1.10×10^{-1} , demonstrating improved long-horizon robustness while preserving nearly the same acceleration as the low-resolution solver. For the vortex shedding frequency, the weak-form correction matches the high-resolution reference, with $St_{\text{weak}} \approx 0.195 \approx St_{u_H}$, whereas the low-resolution solver and strong-form correction underpredict it ($St_{u_L} \approx 0.188$, $St_{\text{strong}} \approx 0.186$). In summary, the weak-form approach provides the best combination of accuracy and efficiency for corrected rollouts.

5 Conclusion

We introduced a differentiable weak-form learning approach to accelerate incompressible finite element simulations by augmenting the momentum equation with learned bilinear operators assembled directly in the variational form. Implemented in Firedrake and trained end-to-end by using discrete adjoints coupled to PyTorch, the approach preserves key numerical structure of the underlying Galerkin discretization. Across the 1D convection–diffusion problem and 2D incompressible Navier–Stokes equations for flow past a cylinder at $Re = 100$, weak-form correction consistently improved rollout accuracy and long-horizon stability relative

to both the uncorrected low-resolution solver and an analogous strong-form correction, while maintaining comparable speedups of $O(10^1 - 10^2)$. In both cases, weak-form learning was more robust to error accumulation in long-horizon rollouts, yielding lower time-averaged relative L^2 error at essentially the same cost as the low-resolution simulation.

Future work will evaluate the proposed approach on additional engineering metrics for the cylinder benchmark, including drag and lift coefficients. We will also explore extending the weak-form correction framework to other applications, assessing generalization across Reynolds numbers and geometries, and scaling training and inference to three-dimensional turbulent flows on unstructured meshes. Finally, we will explore alternative neural architectures for parameterizing the corrective operators, including graph neural networks. An executable reproducibility package (implementation, configurations, and evaluation scripts) is available for verification upon reasonable request.

Acknowledgments

The work was supported by the Argonne Leadership Computing Facility (ALCF) Postdoctoral Fellowship and by the U.S. Department of Energy, Office of Science, Office of Advanced Scientific Computing Research (ASCR) and the Scientific Discovery through Advanced Computing (SciDAC) FASTMath Institute program and Competitive Portfolios Project on Energy Efficient Computing: A Holistic Methodology under Contract No. DE-AC02-06CH11357. JJ thanks Dr. Bethany Lusch for valuable discussions on differentiable training and the implementation of PyTorch.

Author ORCIDs

- ✉ Junoh Jung <https://orcid.org/0000-0003-0962-3127>;
- ✉ Emil Constantinescu <https://orcid.org/0000-0002-7003-6899>.

References

- S. E. Ahmed, O. San, A. Rasheed, T. Iliescu, and A. Veneziani. Physics guided machine learning for variational multiscale reduced order modeling. *SIAM Journal on Scientific Computing*, 45(3):B283–B313, 2023. doi: 10.1137/22M1496360.
- S. Balay, S. Abhyankar, M. Adams, J. Brown, P. Brune, K. Buschelman, L. Dalcin, A. Dener, V. Eijkhout, W. Gropp, et al. *PETSc Users Manual*. Argonne National Laboratory, 2019.
- Y. Bar-Sinai, S. Hoyer, J. Hickey, and M. P. Brenner. Learning data-driven discretizations for partial differential equations. *Proceedings of the National Academy of Sciences*, 116(31):15344–15349, 2019. doi: 10.1073/pnas.1814058116.
- A. Beck, D. Flad, and C.-D. Munz. Deep neural networks for data-driven LES closure models. *Journal of Computational Physics*, 398:108910, 2019. doi: 10.1016/j.jcp.2019.108910.
- D. A. Bezgin, A. B. Buhendwa, and N. A. Adams. JAX-Fluids: a fully-differentiable high-order computational fluid dynamics solver for compressible two-phase flows. *Computer Physics Communications*, 282:108527, 2023. doi: 10.1016/j.cpc.2022.108527.
- D. A. Bezgin, A. B. Buhendwa, and N. A. Adams. JAX-Fluids 2.0: Towards HPC for differentiable CFD of compressible two-phase flows. *Computer Physics Communications*, 308:109433, 2025. doi: 10.1016/j.cpc.2024.109433.
- N. Bouziani and D. A. Ham. Escaping the abstraction: A foreign function interface for the unified form language (UFL), 2021. URL <https://arxiv.org/abs/2111.00945>.

N. Bouziani and D. A. Ham. Physics-driven machine learning models coupling PyTorch and Firedrake, 2023. URL <https://arxiv.org/abs/2303.06871>.

N. Bouziani, D. A. Ham, and A. Farsi. Differentiable programming across the PDE and machine learning barrier, 2024. URL <https://arxiv.org/abs/2409.06085>.

S. L. Brunton, B. R. Noack, and P. Koumoutsakos. Machine learning for fluid mechanics. *Annual Review of Fluid Mechanics*, 52:477–508, 2020. doi: 10.1146/annurev-fluid-010719-060214.

F. Chen, J. Huang, C. Wang, and H. Yang. Friedrichs learning: Weak solutions of partial differential equations via deep learning. *SIAM Journal on Scientific Computing*, 45(3):A1271–A1299, 2023. doi: 10.1137/22M1488405.

E. S. Dar, F. Verdugo, G. Dassi, R. Codina, G. Stabile, and G. Rozza. Artificial neural network based correction for reduced order models in computational fluid mechanics. *Computer Methods in Applied Mechanics and Engineering*, 415:116232, 2023. doi: 10.1016/j.cma.2023.116232.

F. De Avila Belbute-Peres, T. Economou, and Z. Kolter. Combining differentiable PDE solvers and graph neural networks for fluid flow prediction. In *Proceedings of the 37th International Conference on Machine Learning*, volume 119 of *Proceedings of Machine Learning Research*, pages 2402–2411. PMLR, 2020. URL <https://proceedings.mlr.press/v119/de-avila-belbute-peres20a.html>.

F. M. De Lara and E. Ferrer. Accelerating high order discontinuous Galerkin solvers using neural networks: 1D Burgers’ equation. *Computers & Fluids*, 235:105274, 2022. doi: 10.1016/j.compfluid.2021.105274.

T. De Ryck, S. Mishra, and R. Molinaro. wPINNs: weak physics informed neural networks for approximating entropy solutions of hyperbolic conservation laws. *SIAM Journal on Numerical Analysis*, 62(2):811–841, 2024. doi: 10.1137/22M1522504.

Patrick E. Farrell, David A. Ham, Simon W. Funke, and Marie E. Rognes. Automated derivation of the adjoint of high-level transient finite element programs. *SIAM Journal on Scientific Computing*, 35(4):C369–C393, 2013. doi: 10.1137/120873558.

S. W. Funke and P. E. Farrell. A framework for automated pde-constrained optimisation, 2013. URL <https://arxiv.org/abs/1302.3894>.

D. A. Ham, P. H. J. Kelly, L. Mitchell, C. J. Cotter, R. C. Kirby, et al. *Firedrake User Manual*. Imperial College London and University of Oxford and Baylor University and University of Washington, first edition edition, 2023.

A. Ivagnes, J. Wang, M. S. Paci, G. Stabile, R. Codina, and G. Rozza. Pressure data-driven variational multiscale reduced order models for industrial flows. *Journal of Computational Physics*, 476:111904, 2023. doi: 10.1016/j.jcp.2022.111904.

J. Jung and E. M. Constantinescu. Hybrid physics–machine learning framework toward efficient simulation of turbulent flows on an exascale platform. In *APS Division of Fluid Dynamics Annual Meeting 2025*, November 2025. URL <https://archive.aps.org/dfd/2025/c12/13/>. Abstract C12.13 (oral), presented Nov. 23, 2025.

S. Kang and E. M. Constantinescu. Learning subgrid-scale models with neural ordinary differential equations. *Computers & Fluids*, 261:105919, 2023. doi: 10.1016/j.compfluid.2023.105919.

S. Kang and E. M. Constantinescu. Differentiable DG with neural operator source term correction, 2025. URL <https://arxiv.org/abs/2310.18897>.

H. Kim, V. Shankar, V. Viswanathan, and R. Maulik. Generalizable data-driven turbulence closure modeling on unstructured grids with differentiable physics, 2024. URL <https://arxiv.org/abs/2307.13533>.

B. Koc, S. Rubino, T. Chacon Rebollo, and T. Iliescu. Residual-based data-driven variational multiscale reduced order models for parameter-dependent problems. *Computational and Applied Mathematics*, 44:308, 2025. doi: 10.1007/s40314-025-03273-0.

Z. Li, N. Kovachki, K. Azizzadenesheli, B. Liu, K. Bhattacharya, A. M. Stuart, and A. Anandkumar. Fourier neural operator for parametric partial differential equations. In *International Conference on Learning Representations (ICLR)*, 2021. URL <https://arxiv.org/abs/2010.08895>.

J. Ling, A. Kurzawski, and J. Templeton. Reynolds-averaged turbulence modelling using deep neural networks with embedded invariance. *Journal of Fluid Mechanics*, 807:155–166, 2016. doi: 10.1017/jfm.2016.615.

Björn List, Li-Wei Chen, and Nils Thuerey. Learned turbulence modelling with differentiable fluid solvers: Physics-based loss functions and optimisation horizons. *Journal of Fluid Mechanics*, 949:A25, 2022. doi: 10.1017/jfm.2022.738.

J. F. MacArt, J. Sirignano, and J. B. Freund. Embedded training of neural-network subgrid-scale turbulence models. *Physical Review Fluids*, 6(5):050502, 2021. doi: 10.1103/PhysRevFluids.6.050502.

R. Maulik, O. San, A. Rasheed, and P. Vedula. Subgrid modelling for two-dimensional turbulence using neural networks. *Journal of Fluid Mechanics*, 858:122–144, 2019. doi: 10.1017/jfm.2018.770.

C. A. Michelén and H. Xiao. End-to-end differentiable learning of turbulence models from indirect observations. *Theoretical and Applied Mechanics Letters*, 11(4):100280, 2021. doi: 10.1016/j.taml.2021.100280.

Sebastian K. Mitusch, Simon W. Funke, and Jørgen S. Dokken. dolfin-adjoint 2018.1: Automated adjoints for fenics and firedrake. *Journal of Open Source Software*, 4(38):1292, 2019. doi: 10.21105/joss.01292.

C. Mou, B. Koc, O. San, L. G. Rebholz, and T. Iliescu. Data-driven variational multiscale reduced order models. *Computer Methods in Applied Mechanics and Engineering*, 373:113470, 2021. doi: 10.1016/j.cma.2020.113470.

R. W. Nixon-Hill, D. Shapero, C. J. Cotter, and D. A. Ham. Consistent point data assimilation in Firedrake and Icepack. *Geoscientific Model Development*, 17:5369–5386, 2024. doi: 10.5194/gmd-17-5369-2024.

K. Otmani, A. Mateo-Gabín, G. Rubio, and E. Ferrer. Accelerating high order discontinuous Galerkin solvers through a clustering-based viscous/turbulent-inviscid domain decomposition. *Engineering with Computers*, 41(2):949–964, 2025. doi: 10.1007/s00366-024-02062-3.

E. J. Parish and K. Duraisamy. A paradigm for data-driven predictive modeling using field inversion and machine learning. *Journal of Computational Physics*, 305:758–774, 2016. doi: 10.1016/j.jcp.2015.11.012.

J. Pathak, S. Subramanian, P. Harrington, S. Raja, A. Chatopadhyay, M. Mardani, T. Kurth, D. Hall, Z. Li, K. Azizzadenesheli, P. Hassanzadeh, K. Kashinath, and A. Anandkumar. FourCastNet: a global data-driven high-resolution weather model using adaptive Fourier neural operators, 2022. URL <https://arxiv.org/abs/2202.11214>.

T. Pfaff, M. Fortunato, A. Sanchez-Gonzalez, and P. W. Battaglia. Learning mesh-based simulation with graph networks. In *International Conference on Learning Representations (ICLR)*, 2021. URL <https://arxiv.org/abs/2010.03409>.

M. Raissi, P. Perdikaris, and G. E. Karniadakis. Physics-informed neural networks: A deep learning framework for solving forward and inverse problems involving nonlinear partial differential equations. *Journal of Computational Physics*, 378:686–707, 2019. doi: 10.1016/j.jcp.2018.10.045.

F. Rathgeber, D. A. Ham, L. Mitchell, M. Lange, F. Luporini, A. T. T. McRae, G. Bercea, G. R. Markall, and P. H. J. Kelly. Firedrake: Automating the finite element method by composing abstractions. *ACM Transactions on Mathematical Software*, 43(3):1–27, 2016. doi: 10.1145/2998441.

B. Sanderse, P. Stinis, R. Maulik, and S. E. Ahmed. Scientific machine learning for closure models in multiscale problems: A review. *Foundations of Data Science*, 7(1):298–337, 2025. doi: 10.3934/fods.2024043.

M. Schäfer, S. Turek, F. Durst, E. Krause, and R. Rannacher. Benchmark computations of laminar flow around a cylinder. In *Flow Simulation with High-Performance Computers II*, volume 48 of *Notes on*

Numerical Fluid Mechanics (NNFM), pages 547–566. 1996. doi: 10.1007/978-3-322-89849-4_39. URL https://doi.org/10.1007/978-3-322-89849-4_39.

V. Shankar, D. Chakraborty, V. Viswanathan, and R. Maulik. Differentiable turbulence: Closure as a partial differential equation constrained optimization. *Physical Review Fluids*, 10(2):024605, 2025. doi: 10.1103/PhysRevFluids.10.024605.

A. P. Singh and K. Duraisamy. Augmentation of turbulence models using field inversion and machine learning. In *55th AIAA Aerospace Sciences Meeting*, 2017. doi: 10.2514/6.2017-0993.

J. Sirignano, J. F. MacArt, and J. B. Freund. DPM: A deep learning PDE augmentation method with application to large-eddy simulation. *Journal of Computational Physics*, 423:109811, 2020. doi: 10.1016/j.jcp.2020.109811.

T. Tassi, A. Zingaro, and L. Dede'. A machine learning approach to enhance the SUPG stabilization method for advection-dominated differential problems. *Mathematics in Engineering*, 5(2):1–26, 2023. doi: 10.3934/mine.2023032.

R. Vinuesa and S. L. Brunton. Enhancing computational fluid dynamics with machine learning. *Nature Computational Science*, 2(6):358–366, 2022. doi: 10.1038/s43588-022-00264-7.

C. Xie, J. Wang, and W. E. Modeling subgrid-scale forces by spatial artificial neural networks in large eddy simulation of turbulence. *Physical Review Fluids*, 5:054606, 2020. doi: 10.1103/PhysRevFluids.5.054606.

Y. Zang, G. Bao, X. Ye, and H. Zhou. Weak adversarial networks for high-dimensional partial differential equations. *Journal of Computational Physics*, 411:109409, 2020. doi: 10.1016/j.jcp.2020.109409.

Government License (will be removed at publication): The submitted manuscript has been created by UChicago Argonne, LLC, Operator of Argonne National Laboratory (“Argonne”). Argonne, a U.S. Department of Energy Office of Science laboratory, is operated under Contract No. DE-AC02-06CH11357. The U.S. Government retains for itself, and others acting on its behalf, a paid-up nonexclusive, irrevocable worldwide license in said article to reproduce, prepare derivative works, distribute copies to the public, and perform publicly and display publicly, by or on behalf of the Government. The Department of Energy will provide public access to these results of federally sponsored research in accordance with the DOE Public Access Plan. <http://energy.gov/downloads/doe-public-access-plan>.